



HAL
open science

X-ray microtomography reveals the 3D enzymatic deconstruction pathway of raw lignocellulosic biomass

S Blosse, Antoine Bouchoux, C Y Montanier, Paul Duru

► **To cite this version:**

S Blosse, Antoine Bouchoux, C Y Montanier, Paul Duru. X-ray microtomography reveals the 3D enzymatic deconstruction pathway of raw lignocellulosic biomass. *Bioresource Technology Reports*, 2023, 21, pp.101351. 10.1016/j.biteb.2023.101351 . hal-04038634

HAL Id: hal-04038634

<https://hal.science/hal-04038634>

Submitted on 21 Mar 2023

HAL is a multi-disciplinary open access archive for the deposit and dissemination of scientific research documents, whether they are published or not. The documents may come from teaching and research institutions in France or abroad, or from public or private research centers.

L'archive ouverte pluridisciplinaire **HAL**, est destinée au dépôt et à la diffusion de documents scientifiques de niveau recherche, publiés ou non, émanant des établissements d'enseignement et de recherche français ou étrangers, des laboratoires publics ou privés.

X-ray microtomography reveals the 3D enzymatic deconstruction pathway of raw lignocellulosic biomass

S. Blossse^{1,2}, A. Bouchoux², C.Y. Montanier²✉, P. Duru¹✉

In the context of the development of a circular bioeconomy, plant biomass constitutes a vast potential source of renewable molecules of interest. The industrial process essentially consists in using enzymes for its deconstruction. However, we are still lacking a precise understanding of the enzymes' action on such a complex, multiscale porous material. Here, we demonstrate that X-ray microtomography tackles this question in a unique way, making it possible to follow precisely the enzymatic degradation of a model biomass, wheat straw. We perform a thorough analysis of the imaging results over the full length scale of the sample and as a function of degradation time. In particular, we observe the progressive disappearance of specific cellulose-rich cell walls, with distinct 3D heterogeneities in the enzymatic action at different times and length scales. Those 3D pieces of information about the degradation process contrast clearly with those obtained from classical 2D imaging techniques.

¹Institut de Mécanique des Fluides de Toulouse (IMFT), Université de Toulouse, CNRS-Toulouse, Toulouse, France. ²TBI, Université de Toulouse, CNRS, INRAE, INSA, Toulouse, France. ✉email: paul.duru@imft.fr (P. Duru), cedric.montanier@insa-toulouse.fr (C.Y. Montanier).

30 **Keywords:**

31 X-ray microtomography

32 3D imaging processing

33 Wheat straw

34 Plant cell wall

35 Enzymatic hydrolysis

36

37

38 **Highlights:**

39 3D imaging of wheat straw sample by X-ray μ CT, before and after enzymatic hydrolysis

40 Enzymatic action imaged at different times and length scales

41 The enzymatic action concentrates on parenchyma cell walls

42 Extraction of markers for enzymatic degradation from 3D images

43 Highlighting of the 3D heterogeneities of the enzymatic attack

44

45

46

47

48

49

50

51

52

53

54

55

56

57

58

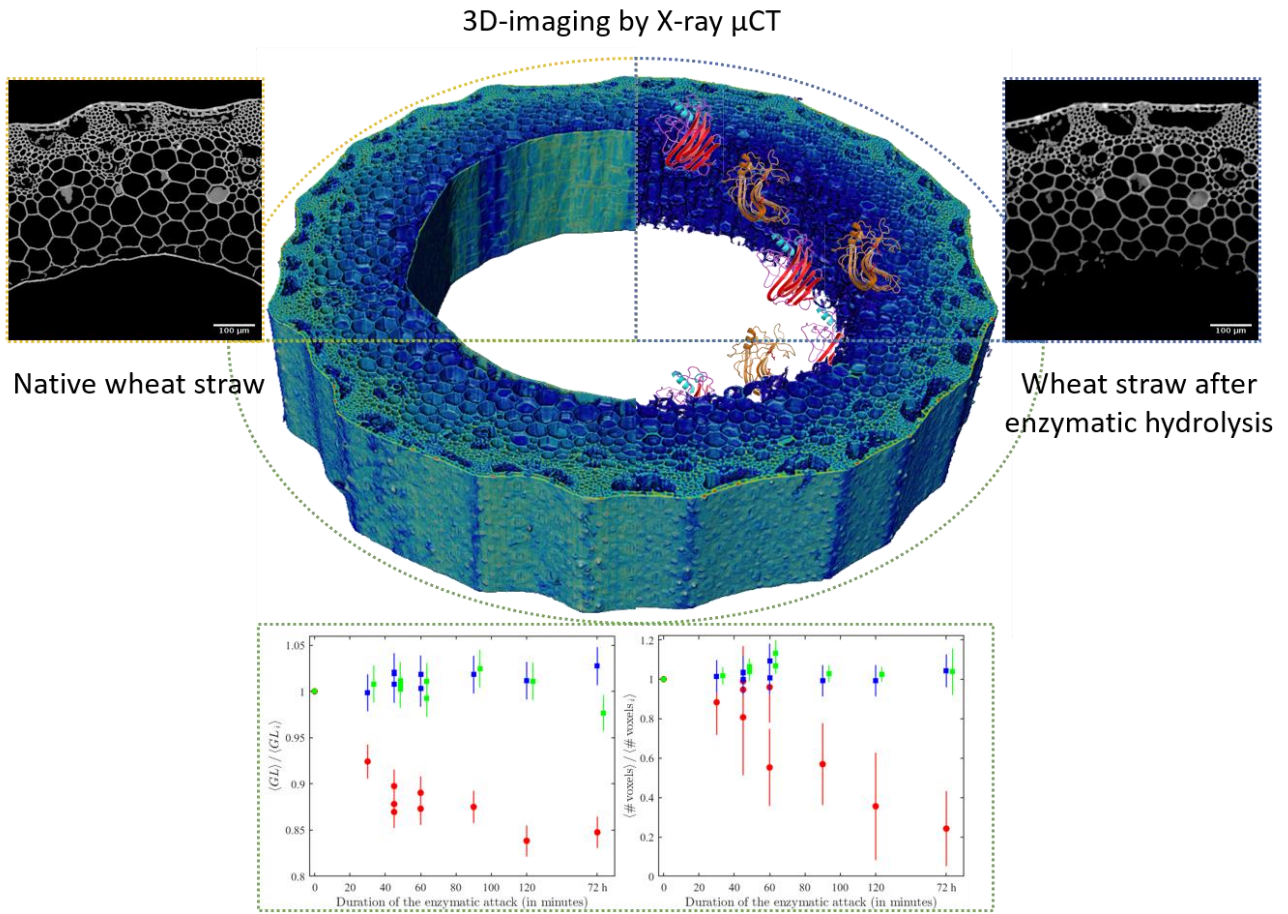
59

60

61 **Graphical Abstract:**

62

63



Markers quantifying enzymatic degradation from 3D image processing

64

65

66

67

68

69

70

71

72

73

74

75

76

77 **1. Introduction**

78 Lignocellulosic biomass, *i.e.*, the cell walls of plants (PCWs), is the largest reservoir of organic carbon
79 on Earth. One huge source of PCW biomass is the by-products of agriculture, which can possibly be
80 used for producing quantities of renewable and sustainable molecules and materials for our daily lives
81 (Cherubini, 2010) For such a valorisation to be performed, lignocellulosic biomass must be
82 decomposed into small elementary pieces, *i.e.*, (macro-)molecules or synthons. This 'deconstruction'
83 process is, however, not an easy task as plants have constantly evolved for protecting themselves from
84 external aggressions (Morris et al., 2018 ; Zhang et al. 2021). This led to PCWs having structures and
85 compositions that are always very complex, even if they obviously vary from one species to another.

86 The average PCW consists in an intricate composite matrix of cellulose, hemicelluloses, proteins
87 and lignin; all components being - covalently or not - linked to each other (Amos and Mohnen, 2019).
88 As we just stressed, this material is highly recalcitrant to chemical or biological degradation. However,
89 cellulolytic microorganisms such as bacteria and fungi also evolved on their side for being able to use
90 the PCW biomass as carbon feedstock. In that case, the attack is performed by lignocellulolytic
91 enzymes that are produced by the microorganisms (Lopes et al., 2018). The enzymes involved are
92 mainly glycoside hydrolases (GHs), a large and diverse group of enzymes that hydrolyse the glycosidic
93 linkages between carbohydrates. GHs include cellulases, hemicellulases and pectinases, as a function
94 of their specificity for a given substrate (Gilbert, 2010).

95 Extensive research has been carried out in the past years with the aim of achieving the enzymatic
96 deconstruction on an industrial scale and designing processes that are economically viable. Studies
97 focus mainly on the research and design of better GHs and on the description of their enzymatic action
98 at the molecular scale. For practical reasons, most of those works are performed using synthetic
99 chromogenic substrates and/or purified polysaccharides (Liberato et al., 2016 ; Gilmore et al., 2020 ;
100 Badruna et al., 2021) . However, this leads to a characterization of the enzymes in conditions that are
101 far from the 'real-life' conditions where enzymes face a raw natural substrate. One first disadvantage
102 of such an approach has to do with the specific recognition interactions that exist between the enzyme
103 and its real substrate and that triggers the catalysis. When using artificial and/or isolated substrates,
104 the conditions for this recognition are not satisfied which can lead to a wrong
105 estimation/understanding of the enzymatic activity towards a real substrate (Montanier et al., 2009).
106 The second downside has to do with the accessibility of the enzyme to its substrate, which is
107 dramatically facilitated using purified polysaccharides as opposed to polysaccharides that are
108 embedded in a PCW.

109 Of course, there have been attempts for tracking and following enzymes' action on a real, natural
110 substrate. Those are mainly microscopy-based studies which, indeed, make it possible to visualize the
111 enzymes and/or the degraded material in conditions that are very close to the real ones (Hervé et al.,
112 2009 ; Zeng et al., 2016 ; Devaux et al., 2018 ; Zoghلامي and Paës, 2019 ; Herbaut et al., 2018) . However,
113 there are still some limitations in those works. The substrate, e.g., corn or tobacco, is often prepared
114 as quasi-2D slices, making it greatly overexposed to the enzymatic attack as compared to the reality.
115 Such 2D-limited approaches do not allow to tackle important questions related to the diffusion and
116 propagation of the enzymes in the material that they degrade. Furthermore, while some microscopy
117 techniques such as confocal microscopy may lead to 3D images of samples with minimal preparation,
118 the true extent of the observation range along the optical axis is always limited, and typically smaller
119 than the characteristic size of the structure in that direction (*e.g.* cell size). It is therefore not
120 straightforward to conclude about the crucial question of the heterogeneity of the degradation in real
121 conditions and at all relevant length scales in the three space directions.

122 Clearly, a major step in the understanding of the enzymatic degradation of PCW biomass would be
123 to visualize the degradation of a raw, natural, material in its three dimensions and using a technique
124 that is less invasive as possible. In this article, we demonstrate that X-ray Computed microTomography
125 (μ CT) is the technique of choice. μ CT is a non-destructive technique that provides 3D images of a
126 sample without any specific preparation, notably without cutting which would lead to exposure of
127 some internal regions of the sample. Laboratory tomography devices (by opposition to synchrotron-
128 based tomography) allow to analyse millimetre-sized samples with a resolution of $\sim 1 \mu\text{m}^3$ in voxel size
129 (Withers, 2007), which is clearly compatible with the dimensions of the PCW features (Hervé et al.,
130 2009). Therefore, μ CT allows to image samples over the 3 directions of space, with a field of view larger
131 than the extent of the typical biomass anatomical feature (the extent of the plant cell in the straw
132 longitudinal direction can be larger than $100 \mu\text{m}$). This is made possible because biomass is transparent
133 to X-ray. Imaging using visible-light sources, such as those used in conventional or confocal microscopy,
134 is typically limited by the limited penetration depth of the light. The literature reports the use of μ CT
135 for exploring plant and wood microstructures (Matsushima et al. 2013; Mathers et al., 2018; Jones et
136 al. 2021; Trtik et al., 2007; Strullu-Derrien et al. 2014; Mayo et al., 2010; Brereton et al. 2015),
137 measuring the swelling properties of wood (Derome et al., 2011), analysing the water content of
138 individual plant cells (Suuronen et al., 2013; Torres-Ruiz et al., 2016), or even localizing mineral
139 particles in sugar cane bagasse (Yancy-Caballero et al., 2017). However, and to the best of our
140 knowledge, μ CT has never been used for investigating the enzymatic deconstruction of a PCW biomass
141 sample.

142 In the present work, wheat straw (WS) is used as a model of both lignocellulosic biomass and
143 agricultural by-product. We first show μ CT 3D images of the raw, native samples, *i.e.*, before any

144 degradation. The general structure of those control samples is briefly discussed, with an emphasis on
145 some specific and little-known features that μ CT is able to detect. We then present the μ CT 3D images
146 of WS samples that have been degraded using a commercial cocktail of lignocellulolytic enzymes at
147 different times. We perform a careful analysis of these images using a procedure that increases in
148 complexity with (i) a first qualitative human-driven analysis of the data, (ii) a computer-driven
149 statistical analysis of the enzymatic degradation course, (iii) a focus on the 3D heterogeneity of the
150 attack as only μ CT can characterize. Our results clearly demonstrate that μ CT is particularly well-suited
151 to reveal the modification of the PCWs within our sample at different stages of the enzymatic
152 deconstruction and that its 3D character is of importance to take into account the complexity of the
153 bioconversion.

154

155

156 **2. Materials & Methods**

157 **Sample preparation**

158 Samples consist in wheat straw (*Triticum aestivum*, cv. Apache, France) intermodal section of 1 cm
159 height, approximately 2 mm diameter and 0.4 mm thickness, harvested in summer 2010 and dried on
160 site. Before using any strands of wheat straw, samples were washed in three successive baths of
161 deionised water for 5 minutes, 10 minutes and one hour, and then dried for 6 hours in a ventilated
162 oven at 45°C.

163 Then, to degrade the wheat straw, a commercial enzymatic cocktail, Novozymes Cellic HTEC2
164 (VHN00003, Luna No. 2010-01668-01), was used at a loading amount of 120 μ g of proteins (\sim 500 μ g
165 of HTEC2 solution) per mg of wheat straw. This cocktail was favored in order to provide an enzymatic
166 activity compatible with an observation of the early stages of the parenchyma cell walls
167 deconstruction. The enzymatic reaction was performed at 45°C under constant agitation at 1000 rpm
168 (ThermoMixer C, Eppendorf) in 2 mL centrifuge tube (1800 μ l of a 50 mM citrate buffer at pH 5.4
169 supplemented with 0.1 mg/mL BSA and 200 μ l of HTEC2 diluted 500 times), during a controlled amount
170 of time (from 30 to 120 minutes). Finally, the samples were dried in a ventilated oven at 45°C for 6
171 hours.

172 The enzymatic activity of the cocktail was determined by dinitrosalicylic acid (DNSA) assays, performed
173 on native samples, to estimate the concentration of reduction sugar equivalent to xylose (Appendix C).
174 Samples were first scanned before enzymatic degradation and then after exposure to the enzymatic
175 cocktail. Preliminary results have shown that exposing twice a given sample to an enzymatic digestion
176 may lead to significant deformation of the sample, certainly provoked by the imbibition and drying

177 procedures involved in the protocol. This precludes the image analysis, which requires to be able to
178 find and follow the same 3D locations in the sample before and after digestion. Consequently, we used
179 multiple native samples, each being subjected to one single enzymatic attack of controlled duration.

180

181 **X-ray micro-CT**

182 Samples were 3D-scanned using a Phoenix Nanotom tomograph, at high spatial resolution, with an
183 isotropic voxel size of 1.25 μm . The distance between the sample axis of rotation and the exit window
184 of the X-ray source was 4 mm. The sample bottom part was partially inserted in a capillary tube with 2
185 mm inner diameter, held by a three-jaw chuck. The top part of the sample was directly exposed to the
186 X-ray beam. Image acquisition was performed at a 45 kV voltage and 250 μA amperage, 1700
187 radiographies were taken with an exposure time of 1250 ms and 4 frames averaging for a total scanning
188 time of around 3 hours. Correction of ring artefacts and reconstruction was performed using the
189 Phoenix Datos|X software. The image analysis detailed in the present paper was performed over a 3D
190 reconstructed volume of 1.25 mm in height, equivalent to 1000 transverse tomographic slices.

191

192

193

194 **Image Processing**

195 The reconstructed 3D volume of the sample was imported into the commercial software Avizo
196 (ThermoFischer Scientific, Waltham, Ma, USA). The first stage of image processing was noise removal
197 using the non-local mean filtering (NLMF) function implemented in Avizo. Filtered tomographic slices
198 were then exported and further processed using Matlab, by performing basic operations over sets of
199 regions of interests located within the 3D image. Volume rendering required a few supplementary
200 steps using Avizo. Segmentation of the image (i.e. separation between the two constitutive materials
201 -air and plant cell walls-) was made using a hysteresis thresholding algorithm and led to a binary image.
202 To remove all the air background, we used the mask function that overlaps the binary image (the mask)
203 and the original grey level (GL) image. Voxels belonging to both the mask and the GL image were
204 retained, together with their GL values, the other being set to zero. Finally, the volume rendering tool
205 was used to obtain the 3D-representation shown in this paper. The image processing workflow, details
206 about the procedures and validation tests are given In Appendix A.

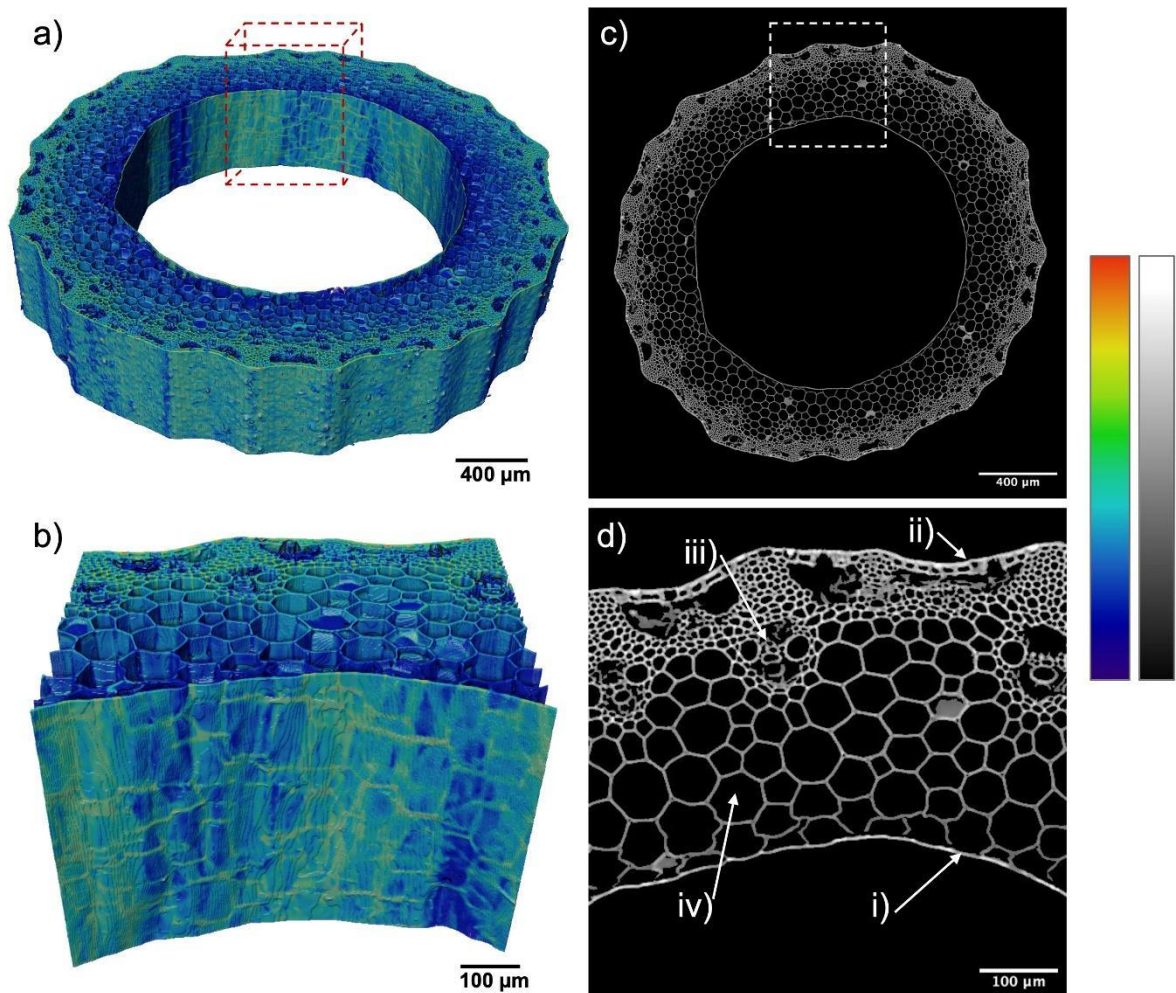
207

208

209 **3. Results and Discussion**

210 **Native wheat straw**

211 All the images showed in this article are obtained using a μ CT Phoenix/GE Nanotom system
212 following a protocol detailed in the Methods section. In Fig. 1, we give the results for one native wheat
213 straw sample, i.e., before any enzymatic treatment. The figure is divided in sub-pictures that together
214 provide a summary of our approach and its performance. Fig. 1a shows the 3D volume rendering of
215 the sample as reconstructed from the μ CT data. Details about the image processing steps are given in
216 the Methods section. The voxel size is $1.25 \mu\text{m}^3$, which is clearly in the high-resolution range of μ CT
217 (Jones et al., 2021; Mayo et al., 2010). The colours of the images correspond to different contrasts
218 between the material and its environment (air). This contrast is roughly proportional to the electron
219 density in the voxels which in turn is related to the average mass density for such biomass samples
220 (Trtik et al., 2007). However, the technique does not allow to exactly quantify the mass density and
221 the colour scale is in arbitrary units. The 3D image of Fig.1a therefore represents the semi-quantitative
222 distribution of the mass density in the material.



223
224 **Fig. 1 μ CT images of native wheat straw.** a) 3D volume rendering (for sake of clarity, only one third of the full
225 reconstructed volume is shown). b) 3D close-up (the front side in the inside wall of the straw, see the dashed red
226 box in a). c) Tomographic transverse slice (taken in the middle of the 3D volume shown in a). d) Close-up of the
227 transverse slice over the dashed white square shown in c). Several anatomical features are indicated: pith cavity
228 lining -PCL- (i), epidermis (ii), large vascular bundles (iii), parenchyma cells (iv). The correspondence between the
229 grey levels of the 2D images and the colormap of the 3D volumes is given on the right.

230

231 The straw has a tubular structure with an inner circular surface that appears smooth at the micron
232 scale. The outer surface is more rugged and presents ~30-50 μm high corrugations that can be
233 associated with a radial elementary pattern of the structure that repeats to form the ring. A 3D close-
234 up that englobes this pattern is given in Fig. 1b. One less impressive but more convenient way to look
235 at these results is to focus on a tomographic transverse slice of the sample (Fig. 1c and the
236 corresponding close-up in Fig. 1d). To facilitate the visualization, such 2D images are given as grayscale
237 images where black has the lowest mass density and white the highest. The main anatomical features
238 of WS are clearly discernible on all these images, especially on Fig. 1d where they are annotated
239 specifically. Different types of cells constitute the structure, with sizes ranging from ~70 μm next to
240 the inner surface, to smaller cells of ~10 μm next to the outer surface. We will not go into a detailed
241 description of the anatomy of WS here as it is already well documented (Nassar et al., 2020; Esau,
242 1960), and we refer the reader to Appendix B (§B.1) for additional details on that point.

243 There are however some interesting aspects that are worth mentioning here and - to the best of
244 our knowledge - are still not reported in the literature. The first one is the fact that the ~7-8 μm width
245 pith cavity lining (PCL) that delimitates the inner surface of the WS particularly stands out with brighter
246 voxels. This higher density of matter in the PCL is not clearly documented in the literature. Additional
247 confocal microscopy images suggest that the PCL is made of a densely packed fibrous structure, which
248 could explain such a high mass density (Appendix B, §B.2). This structure would originate from the
249 formation of the central cavity of the stem when parenchyma cells that form the pith collapse during
250 the maturation of the plant (Kirby, January 2023 from <https://www.fao.org/3/Y4011e/y4011e05.htm>),
251 thus accumulating cellulose-based material and other carbohydrates at this very position. The second
252 striking feature is the mesh-like pattern that we discern on the surface of the PCL on the 3D images of
253 Figs. 1a and 1b. It seems that this structural feature has never been explicitly described before, even if
254 unannotated SEM images previously published suggest similar patterns with WS (Hansen et al., 2011).
255 This pattern, with a mesh size of about the transverse size of a WS cell (~70 μm), is not associated with
256 a rugosity of the inner surface of the wheat straw at the resolution of μCT : it is the presence of voxels
257 with higher mass densities within the PCL that draw this pattern. It does not systematically match with
258 the walls of the cells that are found immediately behind the PCL as is revealed by careful inspection of
259 SEM images and tomographic slices (Appendix B, §B.3). Based on SEM experiments, we show that the
260 mesh results from the presence of a dense, fibrous, mesh-like cellulosic structure within the PCL, that
261 can be revealed when removing the thin external pellicle material that covers the PCL. Again, such a
262 structure is certainly reminiscent of the complex mechanisms that take place during the plant growth,
263 especially during the hollow stem formation, including the probable stacking and squeezing of the cells
264 that eventually form the PCL.

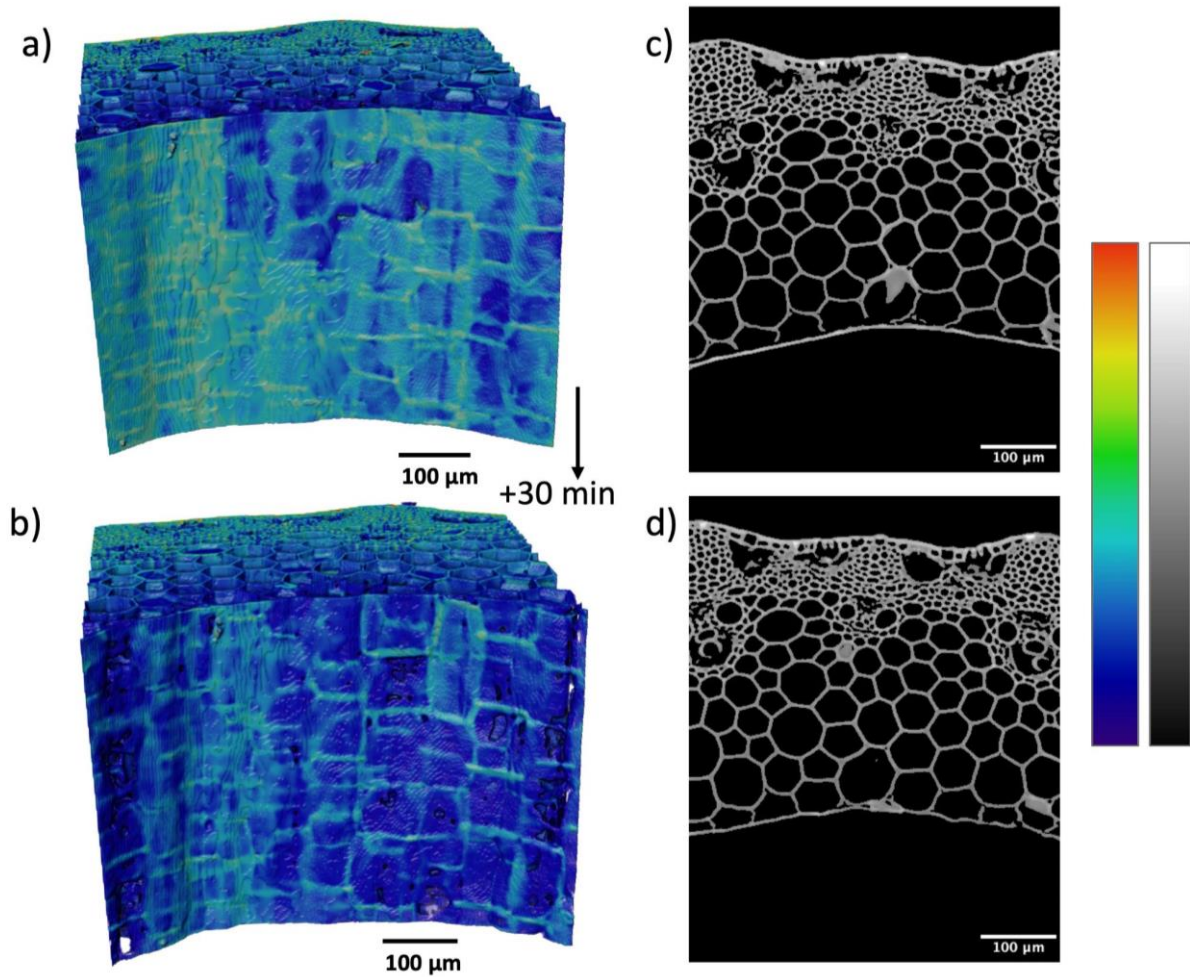
265

266 **Enzymatic degradation of WS as imaged by μ CT**

267 Our approach is an ex-situ approach where the enzymatic treated samples are dried before imaging.
268 As mechanical damage and/or deformation potentially occurs when a same sample is submitted to
269 successive cycles of enzymatic treatment/imaging, we use multiple native samples (see Methods for
270 details). Each one is submitted to the enzymatic cocktail for a given duration and then imaged after
271 drying. The cocktail is a commercial mixture of enzymes (Novozymes A/S) that have complementary
272 activities for the saccharification of generic lignocellulosic substrates, combining enzymes actives on
273 cellulose and on hemicelluloses (Marjamaa and Kruus, 2018) . The different durations of the enzymatic
274 treatment are chosen according to the measurement of the cocktail activity using a chemical
275 procedure detailed in Appendix C. In total, we have six different conditions: five being in a time range
276 where the enzymatic action is clearly measurable and evolves continuously with time (30 min to 2
277 hours), and one 'limiting' case where the WS is exposed to the cocktail for 72 h (see Appendix B, §B.4
278 for details about the preparation of this sample). The analysis then consists in comparing the images
279 obtained for the same sample before and after the enzymatic treatment.

280 Figs. 2-4 provide some significant results of this comparison, with images obtained after 30 min, 1
281 h, and 72 h of enzymatic treatment, respectively. The complete set of images for all the exposure times
282 is given in Appendix B, §B.5.

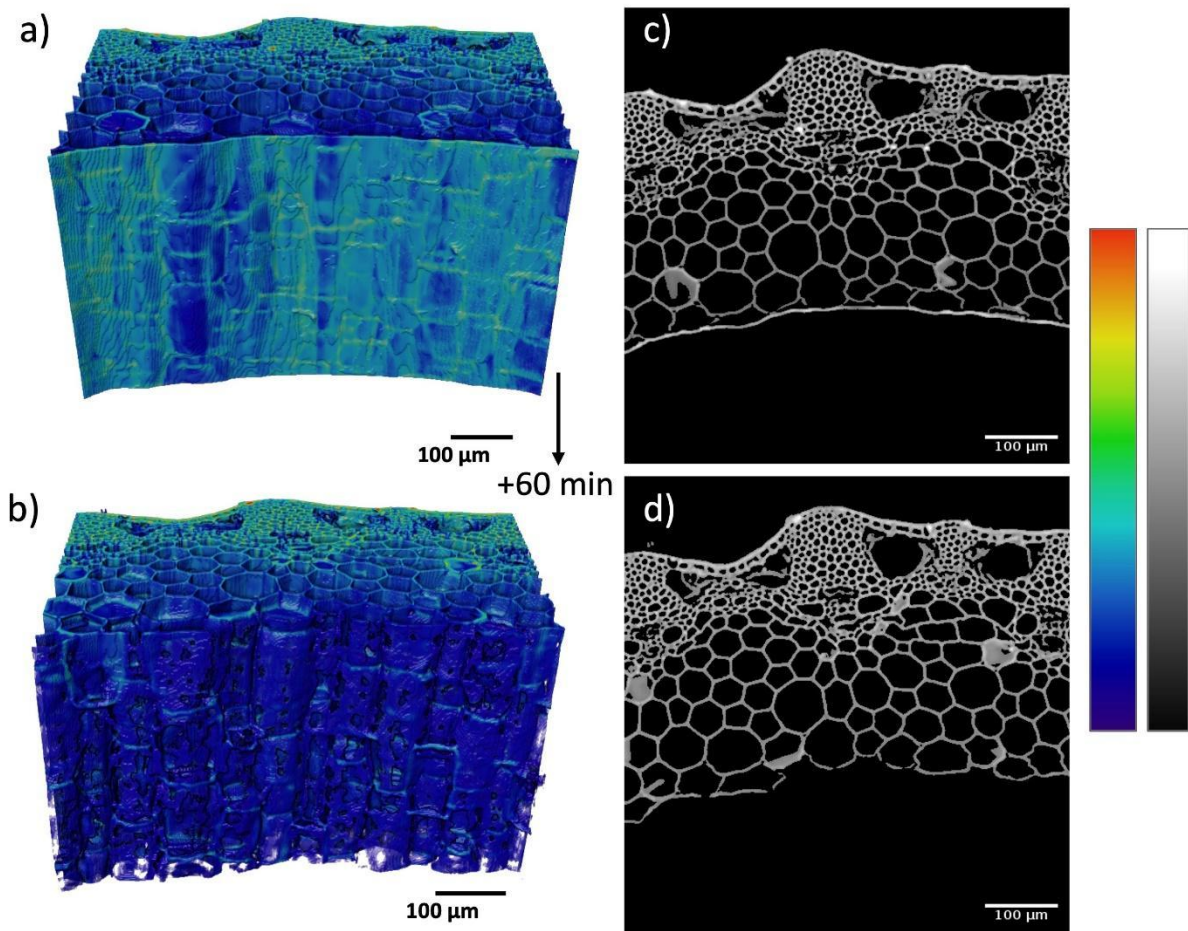
283



284

285 **Fig. 2** μ CT images of wheat straw before and after 30 min of enzymatic degradation. a) 3D volume rendering
 286 before treatment. b) 3D volume rendering after treatment at the same location of the sample. c) Tomographic
 287 transverse slice before treatment. d) Tomographic transverse slice after treatment at the same location of the
 288 sample. The top and bottom images come from different 3D scans but can be compared thanks to the histogram
 289 matching procedure detailed in Appendix A, §A.2.1. As a result, the colormap shown in the right is the same for
 290 the top and bottom images. The procedure for spatial adjustment of the native and digested images is given in
 291 Appendix A, §A.2.2.

292



293

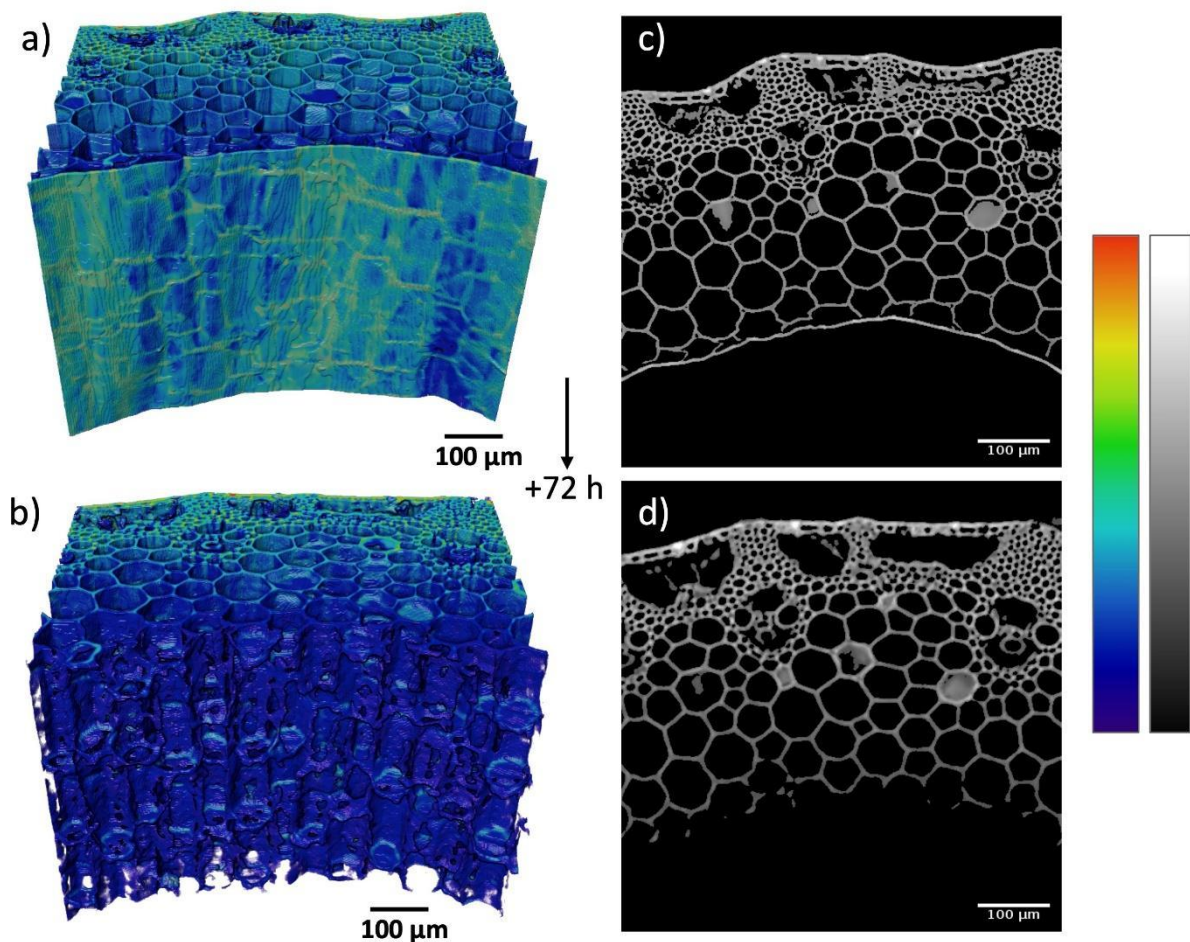
294

295

296

297

Fig. 3 μCT images of wheat straw before and after 1 hour of enzymatic degradation. a) 3D volume rendering before treatment. b) 3D volume rendering after treatment at the same location of the sample. c) Tomographic transverse slice before treatment. d) Tomographic transverse slice after treatment at the same location of the sample.



298

299 **Fig. 4 μCT images of wheat straw before and after 72 hours of enzymatic degradation.** a) 3D volume rendering
 300 before treatment. b) 3D volume rendering after treatment at the same location of the sample. c) Tomographic
 301 transverse slice before treatment. d) Tomographic transverse slice after treatment at the same location of the
 302 sample.

303

304 **General features**

305 A first qualitative and human-driven analysis of these images already gives an interesting picture of
 306 how the deconstruction occurs. After 30 min of enzymatic digestion (Fig. 2), one clearly observes a
 307 decrease in the average voxel intensity, i.e., grey level (GL) value, in the PCL for the digested wheat
 308 straw. On the tomographic slices (Figs. 2c and 2d), the PCL is still present after the enzymatic attack,
 309 but its GL values are now close to those of the internal cell walls. The corresponding volume rendering
 310 confirms this observation (Figs. 2a and 2b), with the PCL that appears blueish over the entire height of
 311 the sample after the enzymatic treatment. However, we still distinguish the mesh pattern of the PCL,
 312 showing that there remain some heterogeneities in mass density. At 1 h of degradation (Fig. 3), the
 313 decrease in GL at the PCL is even more marked. In some places, the PCL is not visible anymore, as
 314 clearly seen in Fig. 3d. This results in the appearance of some 'holes' in the inner structure of the WS,
 315 as shown in Fig. 3b. On the other hand, the initial mesh pattern of the PCL is still identifiable on this

316 picture, meaning that the denser parts of the PCL still resist to the attack at 1 h of degradation. Finally,
317 at 72 h of degradation (Fig. 4), the PCL is totally digested, and the parenchyma cells originally located
318 at the immediate vicinity of the PCL are also attacked. As those cells are now 'opened', this leads to an
319 inner structure that appears hilly and rugged, with a roughness that corresponds to the size of the
320 cells. In the meantime, no enzymatic degradation of the epidermis is evidenced. Overall, these naked-
321 eye observations suggest that the enzymes of the cocktail attack the WS structure from its inner
322 surface, first weaken and then dissolve the PCL, and finally progress into the inner WS structure and
323 degrade it. Apart from that, the human eye is not capable of finding other obvious changes in the μ CT
324 images as the degradation occurs.

325

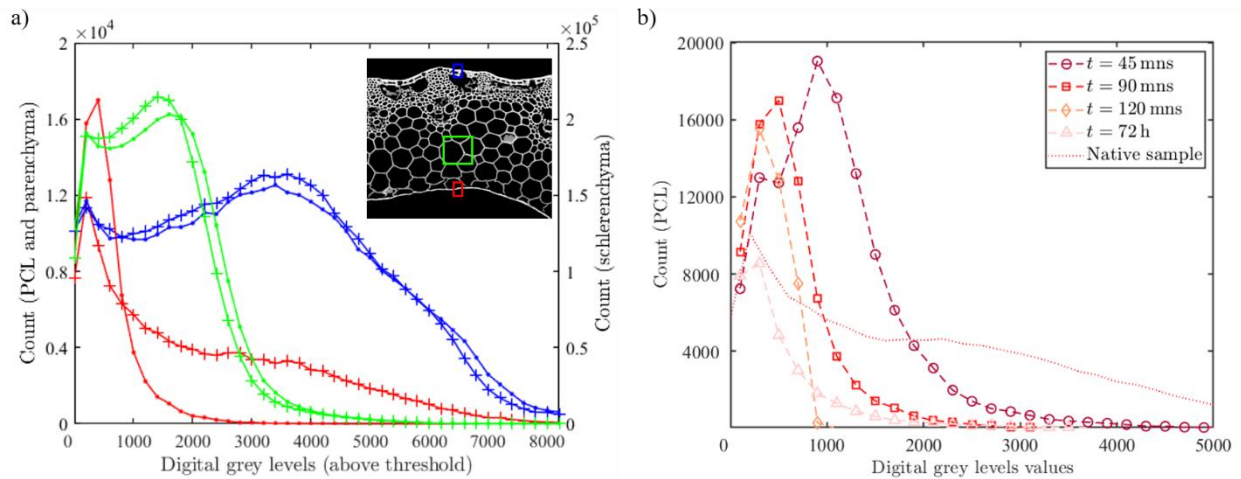
326 **Quantitative markers of enzymatic degradation**

327 For taking a step further in the analysis, a computer-driven examination of the μ CT images is
328 necessary. There are many possible ways to perform such an analysis. Here we focus on a 'coarse-
329 grained' statistical approach aiming at giving a semi-quantitative evaluation of the enzymatic action.
330 The approach consists in defining parallelepiped regions of interest (ROIs) in the samples, based on the
331 changes observed with a naked eye. Three types of ROIs are defined in this way (see the inset in Fig.
332 5a for a schematic representation, full details of the procedure are given in Appendix A, §A.2.3). They
333 correspond to (1) the outer epidermis part (blue), (2) the inner parenchyma part (green), (3) the PCL
334 region (red), with ROI volumes of 1500, 25000 and 1500 μm^3 , respectively. For statistical significance,
335 1000 ROIs are defined for a given sample, each ROI being randomly located along the sample height
336 and circumference.

337 In Fig. 5a, we show the distributions of GLs for all the voxels within a given type of ROI, before and
338 after enzymatic attack. As we are only interested in the mass distribution in the PCW material, the GL
339 values are obtained by subtracting to the raw data the GL value chosen as a threshold to separate the
340 PCW material from air (Appendix A, §A.2.4). The GLs are then divided into classes of equal sizes (200).
341 For visibility, the distributions are not plotted as histograms but as curves where the x-axis values give
342 the centre of each class, and the y-axis the number of voxels in each class.

343 Clearly, the distributions in the epidermis region of the sample (blue curves) are identical before
344 and after the action of the enzymes. In other words, μ CT does not measure any change in mass
345 distribution at those locations in the sample. A similar conclusion can be drawn for the inner
346 parenchyma for which the distributions are also similar before and after treatment (green curves). On
347 the other hand, the results obtained for the PCL regions (red curves) show a strong shift of the
348 distribution towards lower GL values after the enzymatic attack: the GL values in the range [2000-
349 6000], representative of the bright voxels of the PCL in the native image (red crosses in Fig. 5a), are no
350 longer present in the digested sample (red dots). Importantly, such an effect is not found for a control

351 sample that has experienced the same protocol of preparation than the sample of Fig. 5a but in
 352 absence of the enzymatic cocktail (Appendix A, §A.6). This confirms that the evolution of the GLs
 353 distribution observed for the PCL in Fig.5a (from red crosses to red points) is the signature of the
 354 hydrolysis that occurred in the PCL region, for a 90 min treatment in this very case. In Fig. 5b, we focus
 355 on the kinetics of this shift, with results obtained in the PCL regions for different durations of enzymatic
 356 treatment. The obtained distributions are clearly different from one to another, with a progressive
 357 deformation of the distributions towards lower GL values and a significant decrease in the number of

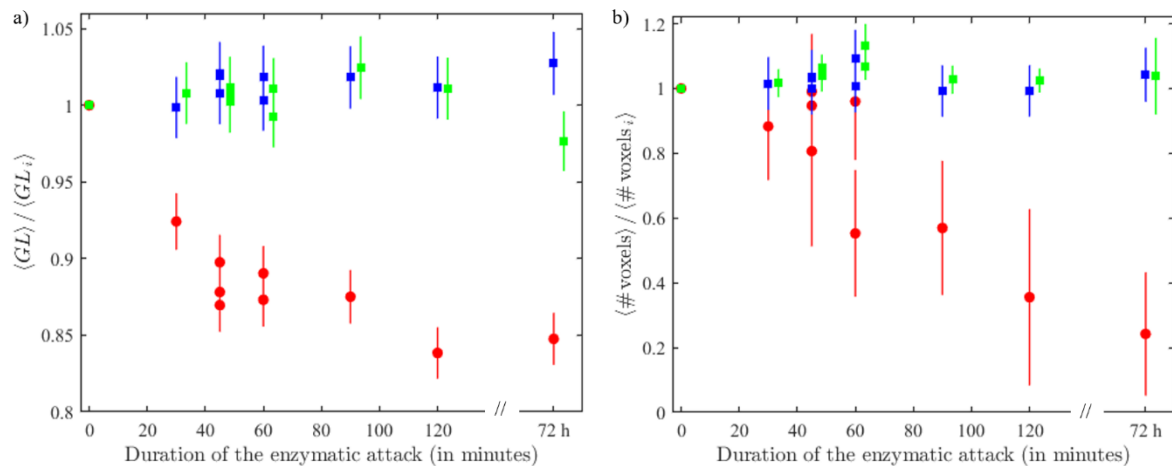


358 PCW material voxels as deconstruction occurs.

359
 360 **Fig. 5 Mass density distribution analysis** a) Grey level distributions before (dots) and after enzymatic attack
 361 (crosses), for a 90 minutes long enzymatic attack. Each colour refers to a given type of ROI, as illustrated in the
 362 inset: across the PCL (red), 125 μm away from the PCL within the parenchyma (green), and across the epidermis
 363 (blue), see Appendix A, §A.2.3 for details. The left y-axis scale is for the PCL (red) and sclerenchyma ROIs (blue),
 364 while the right y-axis scale is for the larger parenchyma ROIs (green). b) Grey level distributions, within the ROIs
 365 located across the PCL (red in Figure 5a), for different duration of the enzymatic attack (see legend). A typical
 366 distribution for a native sample is also shown. The y-axis values are the absolute number of voxels in each class,
 367 meaning that the area below the curve is roughly equal to the total number of voxels belonging to the PCW
 368 material.

369
 370 Generally speaking, two important informative quantities can be extracted from GL distributions
 371 such as those shown in Figure 5: (1) the total number of voxels in the ROIs, which gives a good estimate
 372 of the average volume of PCW material in the boxes, (2) the average GL value in these boxes. In Fig. 6,
 373 we provide the evolution of those two indicators as a function of time for all the samples investigated
 374 and for each type of ROI. Each indicator is normalized by its value before enzymatic degradation, to
 375 get rid of the natural variation between different WS samples.

376



377

378 **Fig. 6 Quantifying the enzymatic deconstruction as a function of time.** a) Mean value of the grey levels for the
 379 voxels belonging to the PCW material, $\langle GL \rangle$, b) total number of voxels belonging to the PCW material, \langle
 380 $\# \text{voxels} \rangle$, as a function of the duration of enzymatic attack. The averaging is performed over 1000 ROIs. PCL
 381 ROIs: red data points, epidermis/parenchyma ROIs: respectively blue and green data points. The latter are slightly
 382 shifted along the x-axis for sake of clarity. For each sample, the data point are rescaled by the value measured
 383 on the native sample ($\langle GL_i \rangle$ and $\langle \# \text{voxels}_i \rangle$). The errors bars come from the uncertainty on the
 384 segmentation threshold (Appendix A, §A.2.4).

385

386 The results of Fig. 6 directly quantify the efficiency of the enzymatic attack and its kinetics and thus
 387 nicely complement the visual inspection of the raw CT images. The markers of Fig. 6a also embed the
 388 main findings of Fig. 5 regarding the PCL: the evolution of the GLs distribution resulting from the
 389 hydrolysis leads to a decrease of the mean value and of the number of voxels belonging to the PCW
 390 material. This is respectively associated with a shift of the GLs distribution towards lower GLs values
 391 and a decrease in the area below the distribution (see Fig. 5.a and 5.b). This is because initially bright
 392 voxels (high GLs) of the PCW material located in the PCL become fainter following the hydrolysis (their
 393 GLs decrease, as also observed in the 3D volume rendering of Fig. 2 to 4) and eventually disappear (this
 394 evolution and its physical interpretation are further discussed in the following). As the contrast
 395 between these voxels and the air background decreases, they are harder to detect on the 3D images
 396 against the air background. Consequently, the uncertainty associated with the choice of the
 397 segmentation threshold is higher than for the others ROIs considered (epidermis and parenchyma), as
 398 shown by the larger errors bars for the total number of PCW material at PCL in Figure 6.b (see Appendix
 399 A, §A.2.4). Two important conclusions regarding the underlying physics of the enzymatic degradation
 400 can be drawn at this stage:

401 . First, regarding the location of the enzymatic attack, the data of Fig. 6 confirm that the enzymatic
 402 degradation essentially proceeds from the PCL, as observed qualitatively on the images. The markers
 403 of the degradation do not exhibit any significant evolution in the epidermis and parenchyma (Fig. 6a
 404 and 6b). Only the PCL is affected by the enzymes both in terms of voxel numbers (total volume) and
 405 average intensity (density). However, we know that the parenchyma cells at the immediate vicinity of

406 the PCL start to be degraded after 1 h of enzymatic treatment (Fig. 4 and S2.5). This is not visible in Fig.
407 6 as those cells do not belong to the parenchyma ROIs that we defined 125 μm away from the PCL. All
408 these findings are in accordance with the results of the literature. For instance, Bertrand *et al.* analysed
409 the decomposition of WS in soil based on biochemical features and histology (Bertrand *et al.*, 2006).
410 As in the present work, only the PCL and parenchyma cells disappear after exposing raw samples to
411 soil microorganisms for 119 days. A similar effect was observed after 8 weeks of composting by
412 Dresbøll *et al.* (2006). In addition, Hansen *et al.* (2013) confirmed that enzymes from commercial
413 cocktails adhere mostly to the PCL and parenchyma cells, making them the most important factor
414 determining WS digestibility. In our case, the rather short durations of enzymatic treatment as
415 compared to the cited studies makes it possible to observe that the PCL is quickly and strongly attacked
416 in the first place, while the parenchyma degrades much more slowly with time. Besides the fact the
417 PCL is obviously the first material that the enzymes encounter during the attack, it therefore seems
418 very likely that the parenchyma material itself is more resistant to the enzyme action than the PCL.
419 This in turn would be due to some - still not so well documented - differences in the structure and
420 chemical composition of both materials. The presence and/or arrangement of lignin in the PCL and
421 parenchyma cell walls is probably one explanation. Lignin, a complex heterogeneous alkyl-aromatic
422 polymer, is embedded in the cellulose/hemicellulose matrix of the plant cell walls, and is indeed known
423 to play a crucial role in the recalcitrance of plants to enzymatic deconstruction (Kim K. H. and Kim C. S.
424 2018). Regarding the epidermis, the absence of observable degradation is due to the high recalcitrance
425 of this anatomical feature, notably due to layers of cutin which is the main component of the
426 epidermis, also named cuticle. This high molecular weight biopolyester is known to embed wax and
427 fats, forming a shield that protects the epidermis from external aggressions as enzymatic attacks
428 (Hansen *et al.*, 2013).

429 . Second, regarding the way the enzymatic attack proceeds at the PCL, the following observations can
430 be made. At the voxel scale, the GL is related to the effective mass density of the PCW material.
431 Therefore, a decrease in the voxel GL can have two different origins: (i) a loss in material (i.e. cellulose
432 and/or hemicellulose), (ii) a local swelling of the microstructure without any loss of material. As
433 evidenced in the images of Figs. 3-4, and quantified in Fig. 6b, the PCL clearly loses some material at
434 time > 60 min and eventually disappears. However, at shorter times (< 60 min), it is possible that the
435 stacked microfibril structure of the cellulose in the PCL (Appendix B, §B.2) may disorganize and then
436 swells under the enzymatic action, occupying a larger space, and thus leading to a less dense -and thus
437 less attenuating- equivalent material at the voxel resolution. This would explain why the average GL of
438 the PCL (Fig. 6a) seems to decrease faster than the number of voxels in the corresponding ROIs (Fig.
439 6b). The evolution of the GLs distribution shown in Fig. 5 would then result from a combination of

440 these two mechanisms: bright pixels that become attenuated induce a shift of the distributions
441 towards lower values, while the loss of material induces a decrease in the number of PCW voxels
442 (decrease of the area below the distribution).

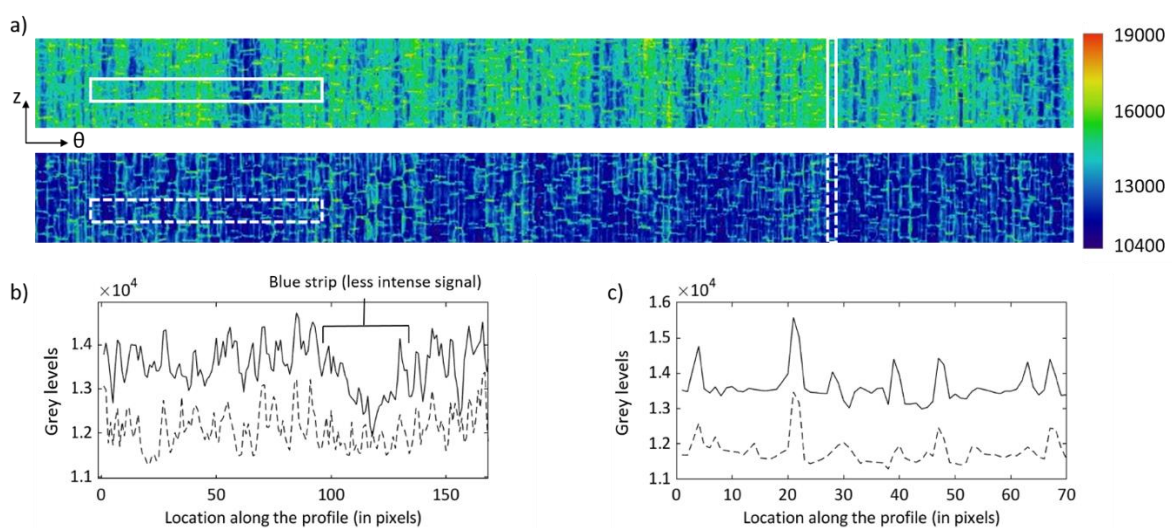
443 The data of Fig. 6b are too noisy to strictly conclude on that point, essentially because of the spatial
444 resolution of the present μ CT images is still not sufficient. However, it seems reasonable to hypothesize
445 that the swelling of the PCL is the first step of the enzymatic degradation, or at least plays an important
446 role at the very beginning of the enzymatic attack. The commercial cocktail used in our study contains
447 hemicellulases, but also a mixture of cellulases (probably endoglucanases (EG), cellobiohydrolases
448 (CBH) and glucosidases), but the precise composition is not provided. EG and CBH are known to
449 penetrate cellulose fibres and pry apart the microfibrils, thus disrupting the fibres surface (Lee et al.,
450 2000). Also, several non-catalytic proteins - that may also compose the commercial cocktail that we
451 used - are involved in changes in the cellulose microfibril structure, such as peeling and disorganization,
452 thus favouring cellulose deconstruction (Arantes and Saddler, 2010).

453

454 **A focus on the 3D heterogeneity of the enzymatic attack**

455 We now go beyond the average, statistical analysis of the μ CT images that we just presented and
456 focus on the structural changes occurring at the PCL at the local scale. To that end, we produce 2D
457 images by 'unrolling' the PCL after paving it with neighbouring parallelepiped-shaped boxes (Appendix
458 A, §A.2.5). A spatial adjustment procedure allows to position the 2D images obtained before and after
459 digestion in the same spatial reference frame (Appendix A, §A.2.2). As we focus on the PCL, this analysis
460 can be performed only if the PCL is not heavily deconstructed, e.g., with missing cellular walls. It is
461 therefore restricted to short durations of exposure to the enzymatic cocktail (≤ 45 min).

462



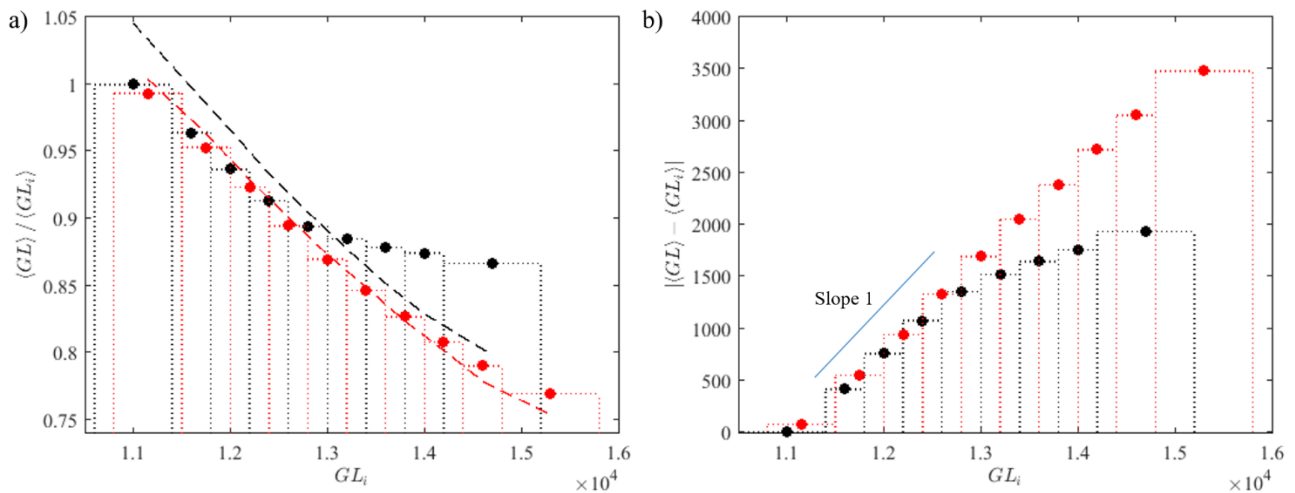
463
464

465 **Fig. 7 PCL degradation at local scale** a) 2D visualizations of the internal surface of a sample before (top) and after
466 (bottom) 45 min of enzymatic attack. The correspondence between the grey levels and the colormap is shown
467 on the right. b) Grey level profiles along the leftmost box, averaged over the box height: native sample (solid line)
468 and digested sample (dashed line). c) Grey level profile along the rightmost box, averaged over the box width:
469 native sample (solid line) and digested sample (dashed line).
470

471 Figure 7a,top is the 2D visualization of the PCL of a native wheat straw, while its digested
472 counterpart is in Figure 7a,bottom. Heterogeneities in mass density can be seen at several scales. At
473 large scale, some darker strips that are roughly aligned with the sample longitudinal axis, and
474 sometimes with varying width, are discernible. A GL profile along the θ direction (leftmost white box)
475 is shown as a solid line in Figure 7b and gives an example of such a large-scale heterogeneity (blue strip
476 position). At smaller scale, the mesh-like network of brighter voxels that we already discussed (see also
477 Appendix B, §B.3) is clearly visible on the images. A profile along the z direction of the rightmost white
478 box displays peaks that correspond to this pattern (solid line in Figure 7c). The main effect observed in
479 the digested image (Figure 7a,bottom) and the profiles extracted from this image (dashed lines in
480 Figure 7b,c) is a global lowering of the GL values. A more careful inspection reveals that the large scale
481 heterogeneities are attenuated after digestion, with a 'smoothing' of the profile in Fig. 7b as if the
482 darker regions were less affected by the enzymatic attack. Another striking feature is that the mesh
483 pattern still remains discernible on the digested sample, but with lower GL values.
484

485 Fig. 7 notably shows that, despite the effect of a 45 min enzymatic treatment, some spatial
486 correlation remains between the 2D images of the PCL before and after the attack. In other words,
487 some of the original heterogeneities in mass density in the PCL appear to be conserved after the attack.
488 We can investigate this more precisely by analysing the change in the GL values as a function of the
489 initial mass density at different positions in the PCL. This is done by dividing the GL distribution in
490 several bins, and then comparing the native ($\langle GL_i \rangle$) and final ($\langle GL \rangle$) GL values averaged over the PCL
491 voxels that initially belongs to each bin. In Fig. 8a, we plot the ratio $\langle GL \rangle / \langle GL_i \rangle$ as a function of $\langle GL_i \rangle$
492 for two enzymatic treatments, i.e., 30 and 45 min (respectively black and red data points). While in Fig.
493 6a we were looking at the evolution of $\langle GL \rangle / \langle GL_i \rangle$ over all the PCW material, here we are investigating
494 the evolution of this parameter at the local scale, based on the initial mass density at distinct regions
495 in the PCL, e.g., the dense mesh-like structure vs the less dense regions (for instance those responsible
496 for the large scale heterogeneities of Fig. 7a,top). In Fig. 8a, the values of the ratio obtained after a
497 random re-ordering of the voxels of the final images are also shown (dashed lines). The observed
498 deviations from the random case indicate a positive correlation between the highest, respectively
499 lowest, GLs on the initial and on the final images. The correlation is clearly marked at 30 min. At 45
500 min, the differences are only significant for the highest and lowest $\langle GL_i \rangle$ and the data clearly tend

501 towards the random case. This suggests a loss of correlation over a large part of the sample, which
 502 corresponds to the disappearance of most of the distinctive structural features of the PCL.
 503



504 **Fig. 8 Analysis of the enzymatic attack heterogeneity** a) Ratio of the GL values after and before enzymatic
 505 attack, $\langle GL \rangle / \langle GL_i \rangle$, as a function of the GLs of the native sample. b) Absolute value of the difference
 506 between the GL values after and before enzymatic attack, $|\langle GL \rangle - \langle GL_i \rangle|$ as a function of the GLs of the
 507 native sample. Each data point is obtained by averaging over all the voxels whose initial GL value belongs to the
 508 corresponding bin, highlighted by the vertical dotted lines. The dashed lines show the result obtained with a
 509 random re-ordering of the image obtained after enzymatic attack. Black, respectively red, lines and data points
 510 are for a 30 min, respectively 45 min, duration of enzymatic attack.
 511

512 Another way of looking at these results is to plot the absolute value of the difference between the
 513 initial and final GL values, $|\langle GL \rangle - \langle GL_i \rangle|$, as a function of $\langle GL_i \rangle$. This representation provides a more
 514 direct view of the process as it gives the actual loss in mass density in the PCL during the enzymatic
 515 attack. One first important observation is that the PCL regions that are initially the less dense (~ 11000
 516 in GL) do not show any loss in mass density as compared to the initial state. This strongly suggests that
 517 the enzymes do not have any activity on those "loose" PCL regions - in the period of time investigated.
 518 The reason for that resistance is less obvious but most probably relies on the fact that the substrate of
 519 the enzymes is absent or is not accessible at these very locations. At higher initial GL values (11000-
 520 13000), the enzymatic action becomes visible with a loss in mass density that increases linearly with
 521 $\langle GL_i \rangle$. It is then clear that the enzymes can work on those denser PCL regions. In addition, the slope of
 522 this linear increase is very close to 1, thus suggesting that the enzymes degrade the PCL until its
 523 structure and composition resemble those of the "loose" regions that we just discussed, at $GL \approx 11000$.
 524 Furthermore, the loss in density is the same at 30 and 45 min of enzymatic treatment, which indicates
 525 that 30 min (or less) is enough to reach that state. At higher initial GL values (> 13000), the loss in mass
 526 density still increases linearly with the initial density in the PCL after a 45 min attack. On the other
 527 hand, the enzymatic digestion of those regions is clearly not complete at 30 min, with losses in mass

528 density that are still lower than at 45 min. For clarity, we recall that Fig. 8 and the associated results
529 are from data obtained before the PCL starts to disappear from the μ CT images ($t < 45$ min) - since a
530 similar local-scale analysis becomes too complicated and risky at higher times. Consequently, the
531 conclusions that we draw are only for that period time, but still suggest that the PCL is attacked by the
532 enzymes until it reaches a given state with a GL value of ~ 11000 . After 45 minutes, the deconstruction
533 mechanism is probably different from a "simple" swelling or loss of material from the structure, with
534 the possible detachment of small pieces of PCL for instance.

535

536 **4. Conclusion**

537 The results of this paper highlight the relevance of X-ray microtomography as a tool to study the
538 enzymatic deconstruction of a typical lignocellulosic biomass, wheat straw. This imaging technique is
539 particularly well-suited to reveal the modification of the plant cell walls within the sample, at different
540 stages of the enzymatic deconstruction, while considering sample heterogeneities in terms of structure
541 and composition at different length scales. In the present case, working with a raw wheat straw
542 sample, enzymatic hydrolysis is shown to proceed progressively from the PCL while the epidermis
543 remains unaffected (at the spatial resolution of the μ CT technique). Markers of the degradation are
544 extracted from a thorough 3D image analysis and can be used to track the kinetics of the hydrolysis.
545 Also, 3D images obtained for a given sample are compared at a local scale, before and after
546 degradation, revealing the heterogeneity of the enzymatic attack, depending on the location on the
547 PCL, a highly heterogeneous anatomical feature, in terms of material density.

548 We believe that this work is a first step in the use of μ CT for understanding the action of enzymes
549 on a real substrate and in real-life conditions. In addition, the analysis that we perform - based on tools
550 and concepts purposely developed for this study - can clearly serve as a μ CT generic workflow for many
551 further works in the field, like studying the action of one or several specific enzyme(s) rather than
552 enzymatic cocktails, and/or the degradation of other types of biomass structures.

553

554

555 **Acknowledgments**

556 We thank Alain Jauneau and Cécile Pouzet for technical assistance on confocal imaging at the TRI-FR
557 AIB imaging platform facility (FR 3450 CNRS-UT3, Castanet-Tolosan, France). We also thank Bruno
558 Payre from the Centre de Microscopie Électronique Appliquée à la Biologie (CMEAB) of the Université
559 Paul Sabatier at Toulouse, France. The research federation FERMAT (Université de Toulouse, CNRS,
560 Toulouse France) is acknowledged for providing access to its X-ray tomography facility.

561

562

563 **Appendixes A, B and C. Supplementary data**

564 Supplementary data to this article can be found online at <https://doi.org/xxx>

565

566 **Funding**

567 This work was partially supported by an internal grant from the French National Research Institute for
568 Agriculture, Food and Environment (INRAE), project Splendid.

569

570 **Author contributions**

571 PD and CYM conceived and designed the experiments. SB and PD performed the experiments. SB, AB,
572 CYM and PD analysed the data. All authors discussed the results and contributed to paper writing.

573

574 **Competing interests**

575 The authors declare no competing interests.

576

577 **Data availability**

578 The data supporting the findings of this study are reported in the main text or the Appendix. Raw data
579 can be obtained from the corresponding authors upon reasonable request.

580

581 **References**

582 Amos, R.A., Mohnen, D., 2019. Critical Review of Plant Cell Wall Matrix Polysaccharide
583 Glycosyltransferase Activities Verified by Heterologous Protein Expression. *Frontiers in Plant Science*
584 10.

585 Arantes, V., Saddler, J.N., 2010. Access to cellulose limits the efficiency of enzymatic hydrolysis: the
586 role of amorphogenesis. *Biotechnology for Biofuels* 3, 4. <https://doi.org/10.1186/1754-6834-3-4>

587 Badruna, L., Burlat, V., Roblin, P., Enjalbert, T., Lippens, G., Venditto, I., O'Donohue, M.J., Montanier,
588 C.Y., 2021. The Jo-In protein welding system is a relevant tool to create CBM-containing plant cell wall
589 degrading enzymes. *New Biotechnology* 65, 31–41. <https://doi.org/10.1016/j.nbt.2021.07.004>

590 Bertrand, I., Chabbert, B., Kurek, B., Recous, S., 2006. Can the Biochemical Features and Histology of
591 Wheat Residues Explain their Decomposition in Soil? *Plant Soil* 281, 291–307.
592 <https://doi.org/10.1007/s11104-005-4628-7>

593 Botany of the wheat plant - E.J.M. Kirby [WWW Document], n.d. URL
594 <https://www.fao.org/3/Y4011e/y4011e05.htm> (accessed 9.5.22).

595 Brereton, N.J.B., Ahmed, F., Sykes, D., Ray, M.J., Shield, I., Karp, A., Murphy, R.J., 2015. X-ray micro-
596 computed tomography in willow reveals tissue patterning of reaction wood and delay in programmed
597 cell death. *BMC Plant Biol* 15, 83. <https://doi.org/10.1186/s12870-015-0438-0>

598 Cherubini, F., 2010. The biorefinery concept: Using biomass instead of oil for producing energy and
599 chemicals. *Energy Conversion and Management* 51, 1412–1421.
600 <https://doi.org/10.1016/j.enconman.2010.01.015>

601 Derome, D., Griffa, M., Koebel, M., Carmeliet, J., 2011. Hysteretic swelling of wood at cellular scale
602 probed by phase-contrast X-ray tomography. *Journal of Structural Biology* 173, 180–190.
603 <https://doi.org/10.1016/j.jsb.2010.08.011>

604 Devaux, M.-F., Jamme, F., André, W., Bouchet, B., Alvarado, C., Durand, S., Robert, P., Saulnier, L.,
605 Bonnin, E., Guillon, F., 2018. Synchrotron Time-Lapse Imaging of Lignocellulosic Biomass Hydrolysis:
606 Tracking Enzyme Localization by Protein Autofluorescence and Biochemical Modification of Cell Walls
607 by Microfluidic Infrared Microspectroscopy. *Frontiers in Plant Science* 9.

608 Dresbøll, D.B., Magid, J., 2006. Structural changes of plant residues during decomposition in a compost
609 environment. *Bioresource Technology* 97, 973–981. <https://doi.org/10.1016/j.biortech.2005.05.003>

610 Gilbert, H.J., 2010. The Biochemistry and Structural Biology of Plant Cell Wall Deconstruction. *Plant*
611 *Physiology* 153, 444–455. <https://doi.org/10.1104/pp.110.156646>

612 Gilmore, S.P., Lillington, S.P., Haitjema, C.H., de Groot, R., O'Malley, M.A., 2020. Designing chimeric
613 enzymes inspired by fungal cellulosomes. *Synthetic and Systems Biotechnology* 5, 23–32.
614 <https://doi.org/10.1016/j.synbio.2020.01.003>

615 Hansen, M.A., Hidayat, B.J., Mogensen, K.K., Jeppesen, M.D., Jørgensen, B., Johansen, K.S., Thygesen,
616 L.G., 2013. Enzyme affinity to cell types in wheat straw (*Triticum aestivum* L.) before and after
617 hydrothermal pretreatment. *Biotechnology for Biofuels* 6, 54. [https://doi.org/10.1186/1754-6834-6-](https://doi.org/10.1186/1754-6834-6-54)
618 54

619 Hansen, M.A.T., Kristensen, J.B., Felby, C., Jørgensen, H., 2011. Pretreatment and enzymatic hydrolysis
620 of wheat straw (*Triticum aestivum* L.) – The impact of lignin relocation and plant tissues on enzymatic
621 accessibility. *Bioresource Technology* 102, 2804–2811.
622 <https://doi.org/10.1016/j.biortech.2010.10.030>

623 Hervé, C., Rogowski, A., Gilbert, H.J., Paul Knox, J., 2009. Enzymatic treatments reveal differential
624 capacities for xylan recognition and degradation in primary and secondary plant cell walls. *The Plant*
625 *Journal* 58, 413–422. <https://doi.org/10.1111/j.1365-313X.2009.03785.x>

626 Jones, D.H., Atkinson, B.S., Ware, A., Sturrock, C.J., Bishopp, A., Wells, D.M., 2021. Preparation,
627 Scanning and Analysis of Duckweed Using X-Ray Computed Microtomography. *Frontiers in Plant*
628 *Science* 11.

629 Kim, K.H., Kim, C.S., 2018. Recent Efforts to Prevent Undesirable Reactions From Fractionation to
630 Depolymerization of Lignin: Toward Maximizing the Value From Lignin. *Frontiers in Energy Research* 6.

631 Lee, I., Evans, B.R., Woodward, J., 2000. The mechanism of cellulase action on cotton fibers: evidence
632 from atomic force microscopy. *Ultramicroscopy* 82, 213–221. [https://doi.org/10.1016/S0304-](https://doi.org/10.1016/S0304-3991(99)00158-8)
633 3991(99)00158-8

634 Liberato, M.V., Silveira, R.L., Prates, É.T., de Araujo, E.A., Pellegrini, V.O.A., Camilo, C.M., Kadowaki,
635 M.A., Neto, M. de O., Popov, A., Skaf, M.S., Polikarpov, I., 2016. Molecular characterization of a family
636 5 glycoside hydrolase suggests an induced-fit enzymatic mechanism. *Sci Rep* 6, 23473.
637 <https://doi.org/10.1038/srep23473>

638 Liu, Q., Luo, L., Zheng, L., 2018. Lignins: Biosynthesis and Biological Functions in Plants. *International*
639 *Journal of Molecular Sciences* 19, 335. <https://doi.org/10.3390/ijms19020335>

640 Lopes, A. m., Ferreira Filho, E. x., Moreira, L. r. s., 2018. An update on enzymatic cocktails for
641 lignocellulose breakdown. *Journal of Applied Microbiology* 125, 632–645.
642 <https://doi.org/10.1111/jam.13923>

643 Marjamaa, K., Kruus, K., 2018. Enzyme biotechnology in degradation and modification of plant cell wall
644 polymers. *Physiologia Plantarum* 164, 106–118. <https://doi.org/10.1111/ppl.12800>

645 Mathers, A.W., Hepworth, C., Baillie, A.L., Sloan, J., Jones, H., Lundgren, M., Fleming, A.J., Mooney, S.J.,
646 Sturrock, C.J., 2018. Investigating the microstructure of plant leaves in 3D with lab-based X-ray
647 computed tomography. *Plant Methods* 14, 99. <https://doi.org/10.1186/s13007-018-0367-7>

648 Matsushima, U., Graf, W., Zabler, S., Manke, I., Dawson, M., Choinka, G., Hilger, A., Herppich, W.B.,
649 2013. 3D-analysis of plant microstructures: advantages and limitations of synchrotron X-ray
650 microtomography. *International Agrophysics* 27.

651 Mayo, S.C., Chen, F., Evans, R., 2010. Micron-scale 3D imaging of wood and plant microstructure using
652 high-resolution X-ray phase-contrast microtomography. *Journal of Structural Biology* 171, 182–188.
653 <https://doi.org/10.1016/j.jsb.2010.04.001>

654 Montanier, C., van Bueren, A.L., Dumon, C., Flint, J.E., Correia, M.A., Prates, J.A., Firbank, S.J., Lewis,
655 R.J., Grondin, G.G., Ghinet, M.G., Gloster, T.M., Herve, C., Knox, J.P., Talbot, B.G., Turkenburg, J.P.,
656 Kerovuo, J., Brzezinski, R., Fontes, C.M.G.A., Davies, G.J., Boraston, A.B., Gilbert, H.J., 2009. Evidence
657 that family 35 carbohydrate binding modules display conserved specificity but divergent function.
658 *Proceedings of the National Academy of Sciences* 106, 3065–3070.
659 <https://doi.org/10.1073/pnas.0808972106>

660 Morris, J.L., Puttick, M.N., Clark, J.W., Edwards, D., Kenrick, P., Pressel, S., Wellman, C.H., Yang, Z.,
661 Schneider, H., Donoghue, P.C.J., 2018. The timescale of early land plant evolution. *Proceedings of the*
662 *National Academy of Sciences* 115, E2274–E2283. <https://doi.org/10.1073/pnas.1719588115>

663 Nassar, R.M.A., Kamel, H.A., Ghoniem, A.E., Alarcón, J.J., Sekara, A., Ulrichs, C., Abdelhamid, M.T.,
664 2020. Physiological and Anatomical Mechanisms in Wheat to Cope with Salt Stress Induced by
665 Seawater. *Plants* 9, 237. <https://doi.org/10.3390/plants9020237>

666 Novy, V., Aïssa, K., Nielsen, F., Straus, S.K., Ciesielski, P., Hunt, C.G., Saddler, J., 2019. Quantifying
667 cellulose accessibility during enzyme-mediated deconstruction using 2 fluorescence-tagged
668 carbohydrate-binding modules. *Proceedings of the National Academy of Sciences* 116, 22545–22551.
669 <https://doi.org/10.1073/pnas.1912354116>

670 Strullu-Derrien, C., Kenrick, P., Tafforeau, P., Cochard, H., Bonnemain, J.-L., Le Hérisse, A., Lardeux, H.,
671 Badel, E., 2014. The earliest wood and its hydraulic properties documented in c. 407-million-year-old
672 fossils using synchrotron microtomography. *Botanical Journal of the Linnean Society* 175, 423–437.
673 <https://doi.org/10.1111/boj.12175>

674 Suuronen, J.-P., Peura, M., Fagerstedt, K., Serimaa, R., 2013. Visualizing water-filled versus embolized
675 status of xylem conduits by desktop x-ray microtomography. *Plant Methods* 9, 11.
676 <https://doi.org/10.1186/1746-4811-9-11>

677 Torres-Ruiz, J.M., Cochard, H., Mencuccini, M., Delzon, S., Badel, E., 2016. Direct observation and
678 modelling of embolism spread between xylem conduits: a case study in Scots pine. *Plant, Cell &*
679 *Environment* 39, 2774–2785. <https://doi.org/10.1111/pce.12840>

680 Trtik, P., Dual, J., Keunecke, D., Mannes, D., Niemz, P., Stähli, P., Kaestner, A., Grosio, A., Stampanoni,
681 M., 2007. 3D imaging of microstructure of spruce wood. *Journal of Structural Biology* 159, 46–55.
682 <https://doi.org/10.1016/j.jsb.2007.02.003>

- 683 Vanholme, R., Demedts, B., Morreel, K., Ralph, J., Boerjan, W., 2010. Lignin Biosynthesis and Structure.
684 *Plant Physiology* 153, 895–905. <https://doi.org/10.1104/pp.110.155119>
- 685 Withers, P.J., 2007. X-ray nanotomography. *Materials Today* 10, 26–34.
686 [https://doi.org/10.1016/S1369-7021\(07\)70305-X](https://doi.org/10.1016/S1369-7021(07)70305-X)
- 687 Yancy-Caballero, D., Ling, L.Y., Archilha, N.L., Ferreira, J.E., Driemeier, C., 2017. Mineral Particles in
688 Sugar Cane Bagasse: Localization and Morphometry Using Microtomography Analysis. *Energy Fuels* 31,
689 12288–12296. <https://doi.org/10.1021/acs.energyfuels.7b02247>
- 690 Zeng, Y., Yarbrough, J.M., Mittal, A., Tucker, M.P., Vinzant, T.B., Decker, S.R., Himmel, M.E., 2016. In
691 situ label-free imaging of hemicellulose in plant cell walls using stimulated Raman scattering
692 microscopy. *Biotechnology for Biofuels* 9, 256. <https://doi.org/10.1186/s13068-016-0669-9>
- 693 Zhang, B., Gao, Y., Zhang, L., Zhou, Y., 2021. The plant cell wall: Biosynthesis, construction, and
694 functions. *Journal of Integrative Plant Biology* 63, 251–272. <https://doi.org/10.1111/jipb.13055>